

Self-consistent simulation of quantum wires defined by local oxidation of Ga(Al)As heterostructures

Christian P. May* and Matthias Troyer†

Institute for Theoretical Physics, ETH Zurich, CH-8093 Zurich, Switzerland

Klaus Ensslin‡

Solid State Physics Laboratory, ETH Zurich, CH-8093 Zurich, Switzerland

(Received 9 October 2007; revised manuscript received 27 November 2007; published 21 December 2007)

We calculate the electronic width of quantum wires as a function of their lithographic width in analogy to experiments performed on nanostructures defined by local oxidation of Ga(Al)As heterostructures. Two-dimensional simulations of two parallel oxide lines on top of a Ga(Al)As heterostructure defining a quantum wire are carried out in the framework of density functional theory in the local density approximation and are found to be in agreement with measurements. Quantitative assessment of the influence of various experimental uncertainties is given. The most influential parameter turns out to be the oxide line depth, followed by its exact shape and the effect of background doping (in decreasing order).

DOI: [10.1103/PhysRevB.76.235321](https://doi.org/10.1103/PhysRevB.76.235321)

PACS number(s): 73.61.Ey, 71.55.Eq

I. INTRODUCTION

There have been several semiconductor quantum dot calculations assuming simplifications such as parabolic confining potentials¹⁻³ and a number of self-consistent solutions of coupled Schrödinger and Poisson equations in III/V semiconductor nanostructures.⁴⁻¹³

However, in particular, the depletion mechanism in two-dimensional electron gases (2DEGs) caused by local oxidation of the surface of AlGaAs/GaAs heterostructures with an atomic force microscope (AFM) has so far only been studied in simplified models assuming a nonrealistic geometry.¹⁴ By AFM induced oxidation,^{15,16} confining walls can be defined with high accuracy enabling long quantum wires with only a few modes. Previous studies on quantum wires have either used analytical approaches,¹⁷ lacked self-consistency,¹⁸ or applied simple geometrical assumptions.¹⁹

In this work, we perform a self-consistent numerical simulation of the effect of oxide lines on top of an AlGaAs/GaAs heterostructure assuming a realistic oxide line profile. In particular, a structure with two oxide lines defining a quantum wire is studied within the framework of density functional theory²⁰ assuming the local density approximation²¹ and the results thereof are compared with available experimental data. The main point of this paper is to treat this specific kind of semiconductor nanostructure on a quantitative level. Moreover, various uncertainties such as background charges are assessed quantitatively in order to rank them by importance and judge their respective influences. Obtaining results for this type of quantum wires which agree with experiments represents a major step toward a full self-consistent simulation of AFM lithography defined III/V semiconductor nanostructure devices such as quantum dots and quantum point contacts with realistic potentials.

II. METHODOLOGY

In order to solve the electrostatic problem, it is necessary to solve Poisson's equation. In our case of a two-dimensional calculation, it reads

$$\nabla(\epsilon(x,y) \nabla) \Phi(x,y) = -\frac{\rho(x,y)}{\epsilon_0}, \quad (1)$$

where ϵ represents the space-dependent dielectricity tensor and ρ denotes the charge density, given by the ionized donor and acceptor concentrations N_n and N_p as well as the electron density n :

$$\rho(x,y) = q(N_n(x,y) - N_p(x,y) - n(x,y)). \quad (2)$$

Furthermore, we solve the one-particle Schrödinger equation

$$\left[-\frac{\hbar^2}{2} \nabla \left(\frac{1}{m^*(x,y)} \nabla \right) + V(x,y) \right] \Psi(x,y) = E \Psi(x,y). \quad (3)$$

In Eq. (3), m^* stands for the space-dependent effective mass, while the potential V consists of the band edge offsets ΔE_c at heterostructure interfaces, the electrostatic potential Φ , and exchange and correlation terms, which are taken into account through the explicit parametrization V_{xc} given by Hedin and Lundqvist,²²

$$V(x,y) = -q\Phi(x,y) + \Delta E_c(x,y) + V_{xc}(\rho(x,y)). \quad (4)$$

The exchange-correlation potential explicitly reads

$$V_{xc}(\rho) = \frac{-2Ry^*}{\pi^{2/3} \left(\frac{4}{9}\right)^{1/3} r_s} \left(1 + 0.7734 \frac{r_s}{21} \log \left(1 + \frac{21}{r_s} \right) \right), \quad (5)$$

where

$$r_s(x,y) = \left(\frac{4}{3} \pi a^*{}^3 \rho(x,y) \right)^{-1/3}, \quad (6)$$

while a^* and Ry^* are the effective Bohr radius and Rydberg constant in the respective material, which are given by

$$a^*(x,y) = 4\pi\epsilon_0\epsilon(x,y) \frac{\hbar^2}{m^*(x,y)q^2}. \quad (7)$$

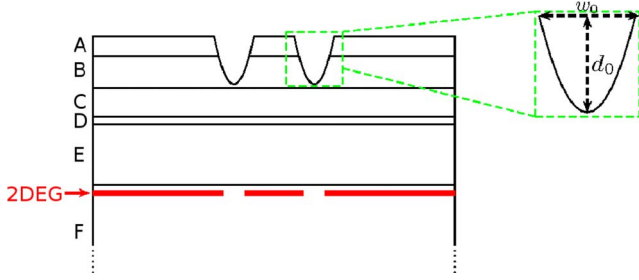


FIG. 1. (Color online) Schematic drawing of heterostructure layout. A: 5 nm GaAs, B: 8 nm $\text{Al}_{0.3}\text{Ga}_{0.7}\text{As}$, C: 7 nm GaAs, D: 2 nm n -doped $\text{Al}_{0.3}\text{Ga}_{0.7}\text{As}$, E: 15 nm $\text{Al}_{0.3}\text{Ga}_{0.7}\text{As}$, and F: bulk GaAs.

$$\text{Ry}^*(x,y) = \frac{q^2}{8\pi\epsilon_0\epsilon(x,y)a^*(x,y)}. \quad (8)$$

Material parameters have been taken from well established sources²³ (the permittivity ϵ of GaAs and $\text{Al}_{0.3}\text{Ga}_{0.7}\text{As}$ is taken as 13.18 and 12.24, respectively, the effective masses of Γ valley electrons, m^*/m_0 , in GaAs and $\text{Al}_{0.3}\text{Ga}_{0.7}\text{As}$ are assumed to be 0.067 and 0.092, respectively, while the conduction band offset between those two materials amounts to $\Delta E_c=0.23$ eV in our simulations).

We discretize both Eqs. (3) and (1) in a finite-difference approach, allowing for different lattice spacings in orthogonal directions.

Equation (3) represents an eigenvalue problem, which we have to solve only in a restricted domain as the electron density equals zero for practical purposes far away from the interface. For computational efficiency reasons, the domain has been chosen to be as small as possible such that it does not change the numerical result compared to the solution within the whole heterostructure domain. Since only the lowest states are needed, the Lanczos algorithm²⁴ is a suitable method for obtaining the eigenstates and their respective energies. We have chosen the freely available IETL (Ref. 30) implementation for this purpose. Having obtained a set of k_{\max} eigenstates Ψ_k allows us to calculate the electron density n by integrating the Fermi distribution multiplied by the density of states of the orthogonal directions over energy. In the case of a two-dimensional simulation, it reads

$$n = \sum_{k=1}^{k_{\max}} |\Psi_k|^2 \int_{E_k}^{\infty} \frac{\sqrt{2m^*}}{\pi\hbar\sqrt{E-E_k}} \frac{1}{1 + \exp\left(\frac{E-E_f}{k_bT}\right)} dE, \quad (9)$$

where E_f and E_k denote the Fermi energy and k th eigenvalue, respectively, while T remains at liquid helium temperatures of 4 K throughout the investigation.

For the solution of Eq. (1), we rely on the biconjugate gradient stabilized method.²⁵ As boundary conditions for the system as depicted in Fig. 1, we demand a vanishing electric field in the bulk (bottom of Fig. 1) and Fermi level pinning on the semiconductor surface.²⁶ The left and right sides of Fig. 1 are connected by periodic boundary conditions, carefully paying attention to choose the lateral extension to be large enough to prevent images of the oxide line potential from having a considerable effect.

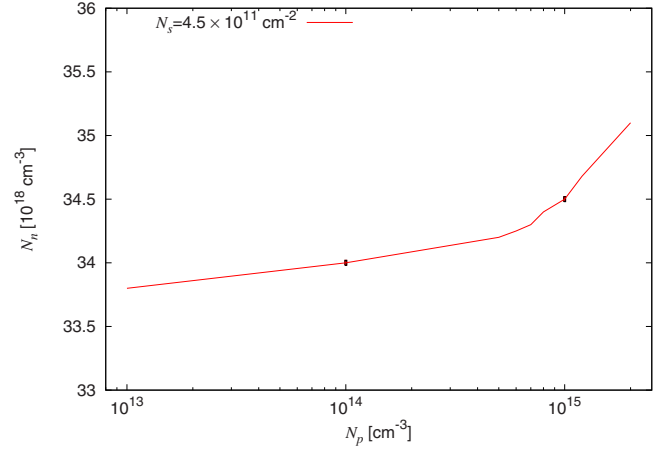


FIG. 2. (Color online) Required modulation n -doping N_n for a given background p -doping N_p yielding a constant sheet density $N_s=4.5 \times 10^{11} \text{ cm}^{-2}$ of the 2DEG.

As both the Lanczos algorithm and the biconjugate gradient stabilized method mainly consist of matrix-vector products, a parallel matrix-vector class has been implemented in order to achieve fast computation and ensure extensibility to three dimensions, which will impose significantly higher computational demands.

Starting with a trial potential, Eqs. (1) and (3) are iteratively solved until a self-consistent solution is found. To ensure convergence, suitable damping schemes²⁷ have to be applied in order to reach the desired equilibrium solution.

The heterostructure we want to investigate is schematically depicted in Fig. 1, following a design which has been realized and characterized experimentally.^{15,28,29} Layer D is n doped in order to generate a 2DEG at the heterostructure interface. However, due to the fabrication process, it is known that the bulk GaAs (denoted F) is usually unintentionally p doped. In our simulations, this results in an additional degree of freedom since for every background doping N_p , a modulation doping N_n can be found that yields the experimentally measured sheet density $N_s=4.5 \times 10^{11} \text{ cm}^{-2}$ of the 2DEG 37 nm below the surface (see later discussion and Fig. 2). This relationship has been established using a one-dimensional self-consistent simulation (without oxide lines) along the growth direction. We then apply the aforementioned numerical method to the structure as defined in Fig. 1, performing two-dimensional simulations in the plane perpendicular to the two parallel oxide lines in order to study the influence of parameter variations on the electronic width of the quantum wire. The latter forms in between the projections of the oxide lines on the 2DEG plane. In the experiment, it has been established that the dimensions of the oxide line below and above the semiconductor surface are approximately the same. It was also demonstrated that the electronic properties of a device confined by oxide lines do not change if the oxide lines are removed, e.g., by HCl etching. Therefore, we use in the following the term “oxide line” to describe the shape of the groove in the semiconductor surface, which leads to a depletion of the electron gas below.

The precise shape and size of the oxide growth under the semiconductor surface cannot easily be probed experimen-

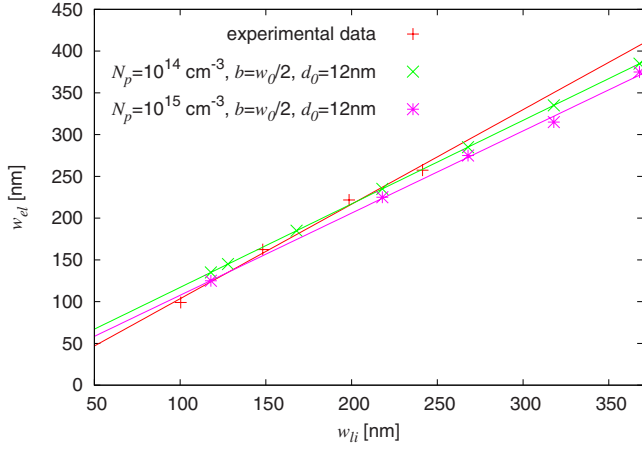


FIG. 3. (Color online) Influence of background doping uncertainty on electronic width: Electronic width w_{el} as a function of lithographic width w_{li} for two simulated cases at constant $b=w_0/2$ and oxide line depth $d_0=12$ nm for different background doping levels N_p (10^{14} and 10^{15} cm^{-3}) as well as experimental values. The symbols denote specifically calculated or measured values; the lines are linear fits to the corresponding data points.

tally. For the exact shape of the oxide line, we therefore choose a Gaussian-like form similar to what has been observed in the experiment.¹⁶ Expressed in terms of the width w_1 as a function of depth d , it reads

$$w_1(d) = 2b \sqrt{-\ln \left[1 + \left(1 - \frac{d}{d_0} \right) (e^{-(w_0/b)^2} - 1) \right]}, \quad (10)$$

where d_0 and w_0 represent the maximum depth and width, respectively, while the parameter b characterizes the width at half-depth.

The main aim of this work is now to assess the influence of these unknown parameters on the electronic wire width quantitatively. In order to obtain independent parameters to vary, we choose a definition of the lithographic width that does not depend on the exact oxide line shape. Following the experiment, we therefore define the lithographic width w_{li} as the horizontal distance of the oxide lines at a depth $d_0/2$ and investigate the influence of relative width b/w_0 , maximum depth d_0 , and background doping N_p , respectively, on the plane defined by the electronic and the lithographic width. The maximum width is kept constant at $w_0=200$ nm throughout the simulations.

III. RESULTS

Experimental electronic width values w_{el} (Refs. 28 and 29) as a function of lithographic width w_{li} are plotted in Figs. 3–5 together with simulations for various parameter settings. In our simulation results, we define the electronic width w_{el} as the spatial distance over which the self-consistent potential is below the Fermi energy. A linear interpolation of the experimental values yields a slope of 1.13 ± 0.07 , while fittings for all simulations result in slopes in the range of

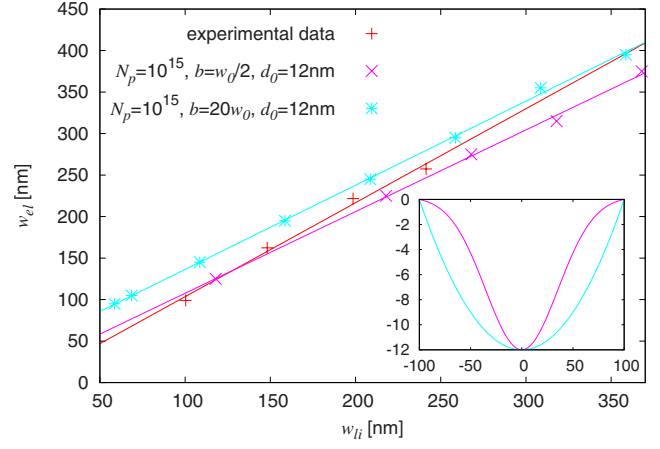


FIG. 4. (Color online) Influence of oxide line shape uncertainty on electronic width: Electronic width w_{el} as a function of lithographic width w_{li} for two simulated cases at constant background doping $N_p=10^{15}$ cm^{-3} and oxide line depth $d_0=12$ nm for different width parameters b ($w_0/2$ and $20w_0$) as well as experimental values. The symbols denote specifically calculated or measured values; the lines are linear fits to the corresponding data points. Inset: geometrical shape of a single oxide line. The same color code as in the electronic width graph has been used to identify the different parameter sets (all axis units are in nanometers).

1.00 ± 0.02 . The experimental error bars have been estimated based on available AFM scans and typical results for the wire width obtained from a fitting of the positions of the minima of the low-field magnetoresistance. The simulation results are within these error bounds.

Since the background doping N_p , the maximum oxidation depth d_0 , and the relative oxide line width b/w_0 are only

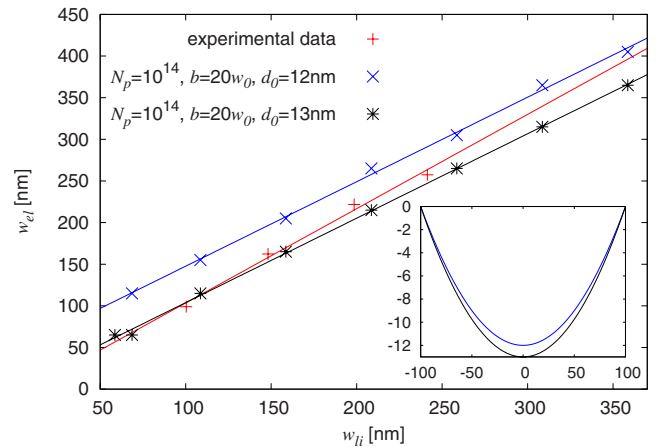


FIG. 5. (Color online) Influence of oxide line depth uncertainty on electronic width: Electronic width w_{el} as a function of lithographic width w_{li} for two simulated cases at constant background doping $N_p=10^{14}$ cm^{-3} and width parameter $b=20w_0$ for different oxide line depths d_0 (12 and 13 nm) as well as experimental values. The symbols denote specifically calculated or measured values; the lines are linear fits to the corresponding data points. Inset: geometrical shape of a single oxide line. The same color code as in the electronic width graph has been used to identify the different parameter sets (all axis units are in nanometers).

known within certain ranges, we now investigate all three of them within their physically meaningful ranges and discuss their respective influences on the electronic width.

In order to assess the influence of the background doping uncertainty, two possible doping concentration combinations (corresponding to the two points marked in Fig. 2) are simulated and their effect on the electronic width is shown in Fig. 3. The effect of the background doping turns out to be of minor importance.

In the following, we choose two extreme cases of possible oxide line shapes, $b=20w_0$, corresponding to a close to rectangular profile, and $b=w_0/2$, which corresponds to the situation where the oxide depth decreases quickly from the center to the edge of the oxide line. All other parameters are kept constant. In Fig. 4, we show the configuration at which the influence of b is largest. It turns out that the choice of b is more relevant for the comparison of experimental and simulated data than the background doping uncertainty.

Finally, all simulations have been carried out at two maximum oxide line depths ($d_0=12$ nm and $d_0=13$ nm), which are most likely to represent the physical reality. Again, Fig. 5 displays the line in configuration space at which the maximum depth exerts the most significant influence leaving all other parameters constant. This parameter turns out to be the crucial one affecting the electronic width as the 2DEG is depleted at larger lateral distances for larger values of d_0 . Figure 5 clearly shows that the minimum lithographic width for the population of the wire, i.e., the value of w_{li} where w_{el} goes to zero, increases with increasing oxide line depth d_0 . For this special case, a situation can be realized where the electronic width w_{el} is larger than zero for a negative value of the lithographic width w_{li} . This peculiar configuration arises because of the definition of w_{li} . This means that the electron gas in the wire can laterally extend significantly under the oxidized areas, an effect which can be confirmed experimentally and is also known from split-gate defined quantum point contacts.

We note that our exploration of the parameter space given by experimental uncertainties does not affect the slope of the electronic width vs lithographic width curve but only adds constant offsets. This fact and the slope of unity we discovered agree with intuition in the case of a lithographic width exceeding all other physical length scales involved. However, on a smaller scale, there should be a higher slope due to screening as well as exchange and interaction effects, which cannot be observed using this oxide line shape because the lithographic width at half-depth is still too wide for these phenomena to have a significant effect. In order to further investigate the behavior at smaller lithographic widths, we therefore implemented another shape allowing for extremely steep oxide line walls, which reads

$$w_2(d) = 2 \sqrt{c_3^2 - \frac{2c_2c_3}{d + c_1}}. \quad (11)$$

We achieve steep walls with the desired oxide distance by choosing the constants $c_1 = -1053/62$, $c_2 = -55575\sqrt{62}/1922$, and $c_3 = 450\sqrt{62}/31$. Figure 6 shows the resulting slope of 3 ± 0.6 for very close oxide lines. This ex-

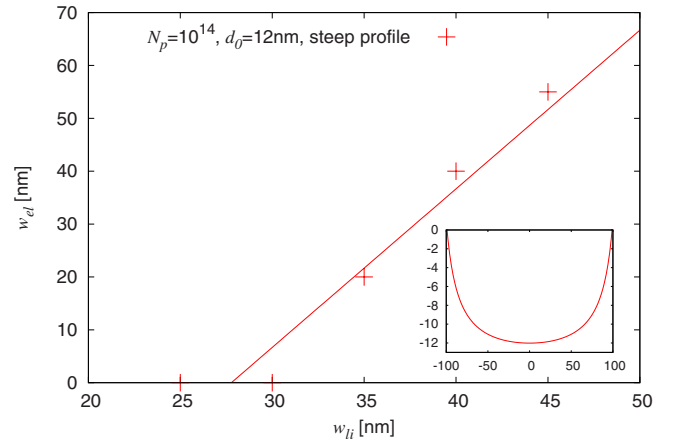


FIG. 6. (Color online) Electronic width w_{el} vs lithographic width w_{li} curve in the small lithographic width limit at background doping $N_p=10^{14}$ cm $^{-3}$ and oxide line depth $d_0=12$ nm with a steep profile (see text). Inset: geometrical shape of a single oxide line (all axis units are in nanometers).

treme choice of parameters is used to test the theoretical limit rather than represent the actual geometry.

Extrapolation down to the intersection of the electronic width vs lithographic width curve with the x axis (lithographic width axis) allows one to read off the physically interesting depletion length. It turns out that moderate parameter variations can easily account for the difference between a positive depletion length (i.e., the quantum wire gets cut off at a finite oxide line distance) and a negative depletion length (it remains conducting).

IV. CONCLUSIONS

Given that experimental error bars are not explicitly taken into account, the simulation data are in reasonable agreement with experiments. Of all parameters investigated, the oxidation depth turns out to be the most influential one. However, also the exact shape of the oxide line, as well as the background doping uncertainty, contributes to the overall error bounds (in decreasing order).

Given the exact physical setup of a nanostructure, the result of electronic width calculations is precisely determined by the well-known laws of quantum mechanics and electrodynamics. Since the exact shape is never exactly known in experiments and also differs from sample to sample, it is not straightforward to calculate the potential profile of more complex geometries.¹⁶ We envision, however, that simulations using the methods presented in this paper will be useful in designing novel structures and in obtaining a better understanding of the electrostatic action of in-plane and top gates. Most importantly, simulations enable us to point out which parameters have the most significant effect. Better experimental control is therefore desirable for these parameters, in this particular case, the oxide line depth.

ACKNOWLEDGMENTS

We thank Jean-David Picon for discussions. All simulations were run on the Beowulf cluster *Gonzales* operated by

ETH Zurich and facilities at the Swiss National Supercomputing Center CSCS. This work was supported by ETH Research Grant No. TH-12 06-3 and the Studienstiftung des deutschen Volkes.

*cmay@itp.phys.ethz.ch

†troyer@phys.ethz.ch

‡enssln@phys.ethz.ch

- ¹C. Metzner and D. Stehr, Phys. Rev. B **70**, 195433 (2004).
²J. Lehmann and D. Loss, Phys. Rev. B **73**, 045328 (2006).
³P. Pietiläinen and T. Chakraborty, Phys. Rev. B **73**, 155315 (2006).
⁴F. Stern and S. DasSarma, Phys. Rev. B **30**, 840 (1984).
⁵G. L. Snider, I.-H. Tan, and E. L. Hu, J. Appl. Phys. **68**, 2849 (1990).
⁶I.-H. Tan, G. L. Snider, L. D. Chang, and E. L. Hu, J. Appl. Phys. **68**, 4071 (1990).
⁷L. R. Ram-Mohan, K. H. Yoo, and J. Moussa, J. Appl. Phys. **95**, 3081 (2004).
⁸L.-X. Zhang and J. P. Leburton, J. Appl. Phys. **96**, 7352 (2004).
⁹D. Jovanovic and J.-P. Leburton, Phys. Rev. B **49**, 7474 (1994).
¹⁰L. Brey, J. J. Palacios, and C. Tejedor, Phys. Rev. B **47**, 13884 (1993).
¹¹D. Schmerek and W. Hansen, Phys. Rev. B **60**, 4485 (1999).
¹²S. E. Laux, A. Kumar, and M. V. Fischetti, J. Appl. Phys. **95**, 5545 (2004).
¹³R. Akis, D. K. Ferry, J. P. Bird, and D. Vasileska, Phys. Rev. B **60**, 2680 (1999).
¹⁴C. May, K. Ensslin, and M. Troyer, J. Comput.-Aided Mater. Des.

14, 91 (2007).

- ¹⁵R. Held, T. Heinzl, P. Studerus, and K. Ensslin, Physica E (Amsterdam) **2**, 748 (1998).
¹⁶A. Fuhrer, A. Dorn, S. Lüscher, T. Heinzl, K. Ensslin, W. Wegscheider, and M. Bichler, Superlattices Microstruct. **31**, 19 (2002).
¹⁷W. Y. Lai and S. Das Sarma, Phys. Rev. B **33**, 8874 (1986).
¹⁸J. Sánchez-Dehesa, J. A. Porto, F. Agulló-Rueda, and F. Measeguer, J. Appl. Phys. **73**, 5027 (1993).
¹⁹Y. Sun and G. Kirczenow, Phys. Rev. B **47**, 4413 (1993).
²⁰P. Hohenberg and W. Kohn, Phys. Rev. **136**, B864 (1964).
²¹W. Kohn and L. J. Sham, Phys. Rev. **140**, A1133 (1965).
²²L. Hedin and B. I. Lundqvist, J. Phys. C **4**, 2064 (1971).
²³I. Vurgaftman, J. R. Meyer, and L. R. Ram-Mohan, J. Appl. Phys. **89**, 5815 (2001).
²⁴C. Lanczos, J. Res. Natl. Bur. Stand. **45**, 255 (1950).
²⁵H. van der Vorst, SIAM (Soc. Ind. Appl. Math.) J. Sci. Stat. Comput. **13**, 631 (1992).
²⁶J. Bardeen, Phys. Rev. **71**, 717 (1947).
²⁷D. D. Johnson, Phys. Rev. B **38**, 12807 (1988).
²⁸R. Held, Ph.D. thesis, ETH, 2000.
²⁹R. Held, S. Lüscher, T. Heinzl, K. Ensslin, and W. Wegscheider, Appl. Phys. Lett. **75**, 1134 (1999).
³⁰<http://www.comp-phys.org/software/ietl/>